COMPUTATIONAL STUDY ON NOISE GENERATION FROM A TWO-WHEEL MAIN LANDING GEAR

Mitsuhiro Murayama*, Yuzuru Yokokawa* and Kazuomi Yamamoto*
***Aviation Program Group, Japan Aerospace Exploration Agency**
murayama.mitsuhiro@jaxa.jp;yokokawa.yuzuru@jaxa,jp;yamamoto.kazuomi@jaxa,jp

Keywords: *aeroacoustics, airframe noise, landing gear*

Abstract

This paper presents recent computational studies by JAXA on landing gear noise using a two-wheel main landing gear research model. The obtained knowledge and findings about the basic flow structures and the main noise sources around the two-wheel landing gear model, the detail flowfields and noise generation mechanisms around the tire-axle region, the sensitivities of detail parts around the tire-axle region to the flowfield and noise level, and the flowfields with two types of low noise devices are discussed by a series of the computational studies.

1 Introduction

Due to recent increasing interest in the environmental problems and anticipated tightening of regulations for aircraft noise around airports, the noise prediction and reduction technology has become one of the key technologies for development of future commercial aircraft. In recent years, the development of low-noise, very high bypass ratio fan jet engines has made the airframe noise stand out in the overall noise level, especially during approach where engines are throttled down [1-4]. The noise from landing gears is known to be one of the major sources of the airframe noise besides the noise from high-lift devices such as slat and flap. The landing gear mainly consists of an assembly of a number of bluff components. The noise from landing gears is basically broadband noise by turbulent vortex shedding from the structures, interaction of turbulent wake among components, and interaction of shear layer from gear bay [1-4]. To reduce the noise effectively, the noise generation mechanism from each noise source with complex turbulent flow interactions should be well understood.

Studies about landing gear noise have been conducted mainly by wind tunnel test and flight test [5-8]. The studies have been mainly conducted on four- or six-wheel type landing gears for large aircrafts and have not been well conducted on two-wheel type main landing gears especially for regional jets with wing-mounted engines. For the research of two-wheel landing gears, NASA has conducted experimental and computational researches on the landing gear of G550 [9-12] collaborating with industries and universities. JAXA has also conducted experimental and computational research work on noise generation mechanism and reduction technologies about two-wheel main landing gears for regional jets since 2008 [13-17] using a 40% scale landing gear experimental research model. The basic characteristics and the main noise sources have been investigated by the experimental and computational researches. It was shown that the tire-axle region has the largest contribution to the noise level, then the detail investigations on the noise generation from the tire-axle region has been conducted. In addition, the low-noise fairings around tire-axle regions have been investigated. This paper provides overview of the obtained knowledge and findings about the noise sources and the low noise devices around the two-wheel main landing gear by a series of the computational studies with the results of recent paper [13,15,17].

2 JAXA's Noise Research Model for Two-wheel Main Landing Gear, LEG

The research model geometry is designed based on the current two-wheel landing gears design methodology for modern 100-passanger class regional jets with wing-mounted engines by a landing gear manufacturer in Japan [13]. The model is called "LEG (Landing gear noise Evaluation Geometry)". Figure 1 shows the main landing gear model.

The wind tunnel testing model was fabricated as 40% scale size. The height and tire-diameter are about 1.2m and 0.4m, respectively. The wind tunnel testing model includes all detail components such as hydraulic brake caliper, small-links, small-pins, electrical wirings, and hydraulic tubes to reproduce the flowfields and resultant noise from actual landing gear. The model can change its configuration from a simple cylindrical main strut to the most complicated geometry equipped with all the components, "fully-dressed configuration" by removing and attaching components to assess the contribution of each component to overall noise level. A cavity for the gear bay to store the landing gear on the wing was modeled by keeping equivalent volume, while the storage space on the fuselage was not included.

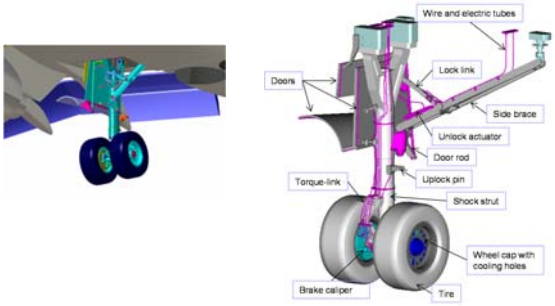

Fig. 1. JAXA noise research model for two-wheel main landing gear, LEG.

3 Experimental Facilities and Measurements

In this research, two different wind tunnel facilities were used, the JAXA's lowspeed wind tunnel (JAXA-LWT2) and the large-scale low-noise wind tunnel of the Railway Technical Research Institute (RTRI).

JAXA-LWT2 as shown in Fig. 2(a) was used for aerodynamic measurements, flowfield measurements by oil-flow and stereo scopic three-dimensional PIV [15], and noise survey with two phased arrays on test section walls. It is an atmospheric pressure closed-circuit tunnel with a solid wall square test section. An anechoic closed test section with Kevlar wall can be used in JAXA-LWT2 [18], but the results in solid wall test section are shown in this paper. The size of the test section is 2m in height, 2m in width, and 4m in length. The noise source localization was conducted with phased arrays that consist of 48 microphones within 1m diameter.

The far-field noise was measured using Large-Scale Anechoic Wind Tunnel in Railway Technical Research Institute (RTRI) [19]. The closed circuit tunnel has an open-jet nozzle with a rectangular cross-section as shown in Fig. 2(b). The size of the test section is 3m in width, 2.5m in height, and 8m in length. 1/4-inch omni-directional microphones with frequency range of 4Hz to 100 kHz were used for the far-field sound measurements. A traversable linear array with five microphones was placed 5m above the axle of the model to measure the directivity of the noise radiation.

Most measurements were conducted under conditions with zero angle of attack (α) and zero side-slip angle (β) at freestream velocity, U_{inf}, of 54.4m/s, which is typical local flow velocity around a main landing gear at approach condition of the assumed aircraft. The measured model-scale Sound Pressure Level (SPL) was scaled to aircraft-scale SPL with the following relationships assuming a constant Strouhal number;

$$SPL_{Aircraft} = SPL_{Model} + 60\log\left(\frac{U_{Aircraft}}{U_{Model}}\right) + 20\log\left(\frac{L_{Aircraft}}{L_{Model}}\right) - 20\log\left(\frac{R_{Aircraft}}{R_{Model}}\right) \quad (1)$$

where $U_{Aircraft}$, $L_{Aircraft}/L_{Model}$ and $R_{Aircraft}$ are 54.4m/s, 2.5, and 120m, respectively. The frequency was also scaled using freestream velocity and unit length. OASPL at aircraft-scale was evaluated integrating the 1/3octave band SPL within a frequancy range from 50Hz to 10kHz in the aircraft-scale. For the comparison of the spectra of SPL with computational results, the background noise in the wind tunnel is subtracted in the experimental data.

(a) Phased arrays in JAXA-LWT2

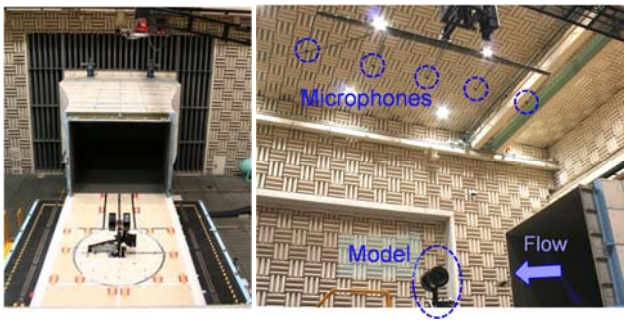

(b) Far-field measurement in RTRI

Fig. 2. Landing gear model and wind tunnels

4 Computational Method

For steady RANS computations to investigate the basic flow fields, an unstructured grid flow solver, TAS-code [20-22], and mixed-element grid generators, TAS-Mesh and MEGG3D [23-27], were used, which are one of the commonly-used CFD codes in JAXA. TAS-code solves RANS equations with second-order spatial accuracy in space. A variant of Spalart-Allmaras one-equation turbulence model, SA-noft2-R (Crot = 1) is used here. Figure 3 shows the cross-sectional view of the volume mesh of a typical unstructured grid. The minimum grid spacing is set to 1.9×10^{-3} mm. The total number of grid points varies from 5 million to 30 million depending on the model complexity.

To investigate detailed aeroacoustics, Very Large Eddy Simulation (VLES) was conducted with a CFD/CAA software, PowerFLOW. The computational method is based on a Lattice Boltzmann Method [28-29]. The system of equations is solved on a Cartesian mesh using a renormalization group-based VLES two-equation turbulence model with an extended turbulent wall model, which allows easy grid generation for highly complex geometries to simulate wall boundary layer with much less grid resolution near wall.

The far field results are obtained with the FW-H method using the model surface pressure including the ground plane which size is the same with one used in the wind tunnel test. SPL in the computations is evaluated at corrected microphone locations considering the advection by free-stream velocity because the microphones are not located in the free-stream at open-cart test. The influence of the refraction by the shear layer due to open-cart test is not considered in the correction.

Figure 4 shows the typical computational grid. The computational grid consists of a total of 8 levels of Variable Resolution (VR). The minimum spacing is set to 0.48mm, which is much larger than that of RANS computations on unstructured grids due to the usage of wall function. The total number of voxels varies from 100 million to 170 million depending on the model complexity. The computations were conducted at U_{inf} = 54.4m/s with α=0 and β=0. The computational Δt was set to 8×10^{-7}[sec]. The total number of time step was about 350000, which corresponds to computations for 0.28[sec].

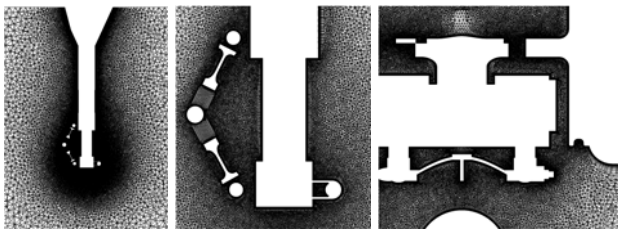

Fig. 3. Cross-sectional views of a typical unstructured grid for RANS computations.

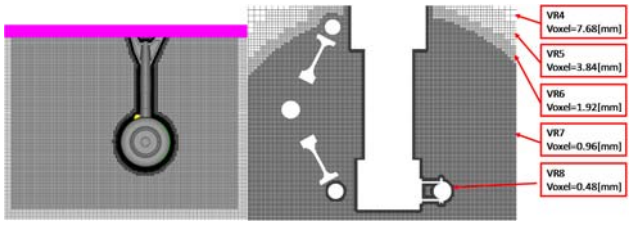

Fig. 4. Cross-sectional views of a typical grid for LES computations.

5 Results

5.1 Main noise sources on fully-dressed configuration

Figure 5 shows noise source localization results for the fully-dressed configuration measured in JAXA-LWT2 [13]. Remarkable noise sources are identified at the center of the model for both Area 1 and Area 2. The region around the bogie and the junctions between the main cylindrical strut and the door and/or the side-brace could be strong noise sources. The side-brace is identified as the prominent noise source at high frequency range especially around junction between side-brace and lock-link. Some door parts are also identified as the dominant noise sources. Figure 6 shows contribution ratio of model components to SPL roughly estimated by attaching and removing model components [13]. "Cylinder+Axle+Tire" shows the largest contribution to the noise generation for most frequency range. Its extremely strong contribution around 0.2kHz is not essential because it was found to be an Aeolian tone noise from a simplified pin in the bogie structure of the wind tunnel model. The peak disappears after the shape change from the simplified pin to the exact one [13]. The "Cylinder+Axle+Tire" could not split each other due to their strong interactions. "Side-brace" showed the second largest contribution.

Figure 7 compares spectra of SPL at a microphone location right above the model between experimental and computational results. The computational result shows good agreement with experimental data up to 1kHz then gradually decreases its level due to limit of the resolving vortex scale. Figure 7 also compares the computational result for the partially-dressed configuration without wirings, tubes and gear bay to investigate their influences. Major differences between the fully-dressed and the partially-dressed configurations are found at the frequency range from 40Hz to 400Hz. As shown in Fig. 6, the difference around 100Hz is considered to be influence of the gear bay.

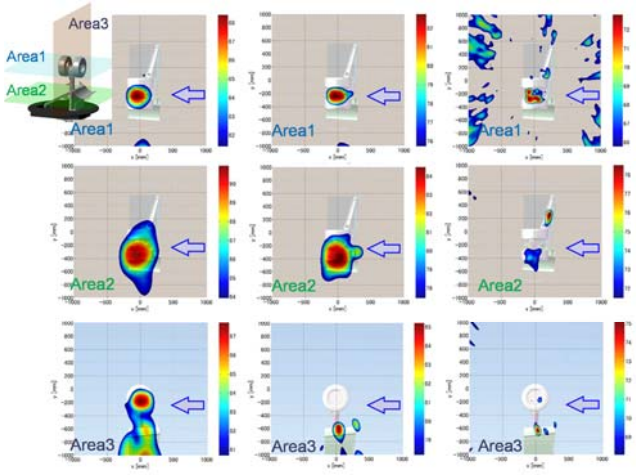

(a) 1kHz (b) 1.6kHz (c) 3.2kHz

Fig. 5. Noise source localization results for the fully-dressed configuration in JAXA-LWT2.

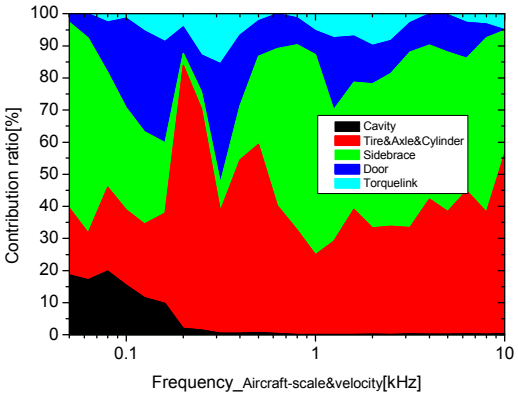

Fig. 6. Rough estimation of contribution ratio of model components to SPL.

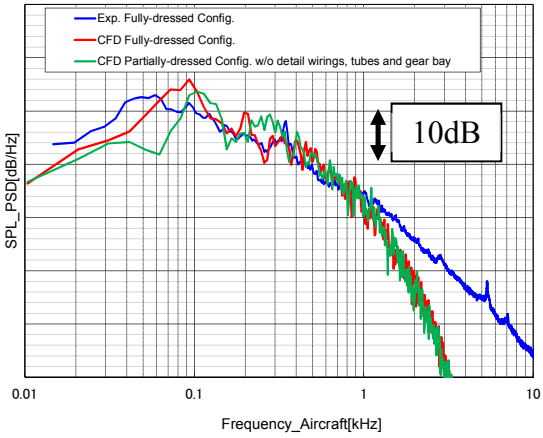

Fig. 7. Comparison of spectra of SPL at a microphone location right above the model between experimental and computational results for the fully-dressed and partially-dressed configrations.

Figure 8 compares the bandpass-filtered pressure fluctuation level in dB of the fully-dressed configuration for the frequency ranges of 141-283Hz and 566-1131Hz. Figure 9 shows the instantanious velocity field and the bandpass-filtered *Cp* in space around the side-brace and gear bay. Figures 10 and 11 shows the results of the partically-dressed configuration. By the computational results, possible noise sources on the tire-axle region, side-brace, and doors corresponding to the experimental results shown in Figs. 5 and 6 can be identified. As for the tire-axle region, the regions with high pressure fluctuation level are found around the inside edges on the back side of tires, the rear part of the side surface of tires, and the junction between the center cylindrical strut, the piston, and torque-link. The detail parts of wiring and tubes seem to have limited impacts around the tire-axle region. The details about the flowfields and noise sources around the tire-axle region, which has the largest contribution to the noise generation, are discussed in the next section.

As for the side-brace, the separated flows from the fore part of the side-brace and lock link basically cause high pressure fluctuation around rear-parts of the side brace and lock link as shown in Figs. 9 and 11. The pressure fluctuation is higher at low frequency range. The regions with high pressure fluctuation level are found especially around the junction between the side-brace and lock-link, the junction between the side-brace and center cylindrical strut, and the unlock actuators at both low and high frequency ranges. In Fig. 9 for the case with the gear bay cavity, high pressure fluctuation regions are found due to the shear layer by the gear bay cavity. The comparison between Figs. 8 and 10 clearly shows that the interaction of the shear layer with the side-brace generates strong pressure fluctuation on the surface of a part of the side-brace.

As for the doors, protuberant door operating rod causes strong pressure fluctuation as is also identified by noise source localization in Fig. 5. The pressure fluctuation on the door surfaces is also higher at low frequency range.

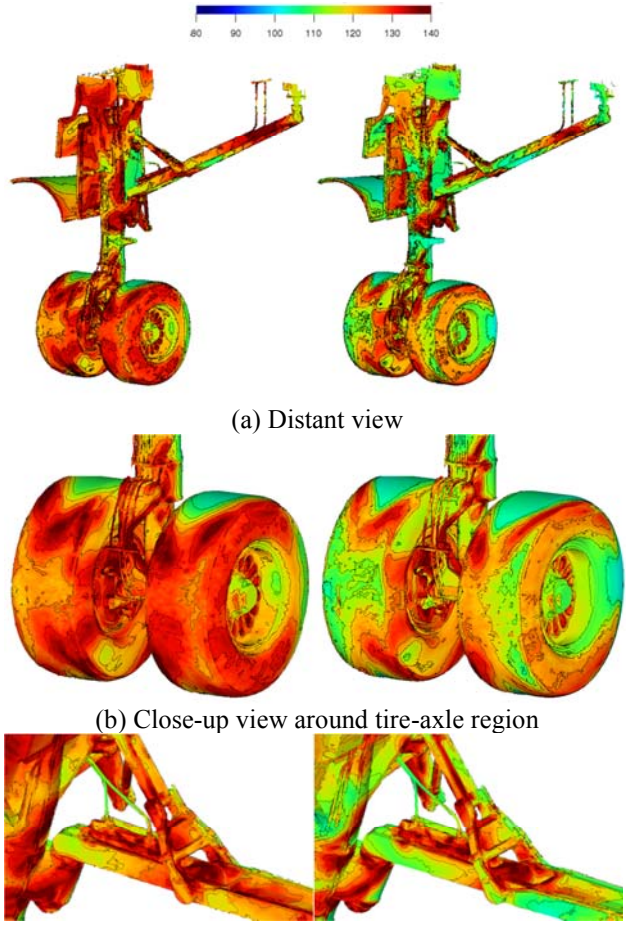

(a) Distant view

(b) Close-up view around tire-axle region

(c) Close-up view around junction between side-brace and lock-link

Fig. 8. Comparison of the bandpass-filtered pressure fluctuation level in dB of the fully-dressed configuration (left: 141-283Hz, right: 566-1131Hz).

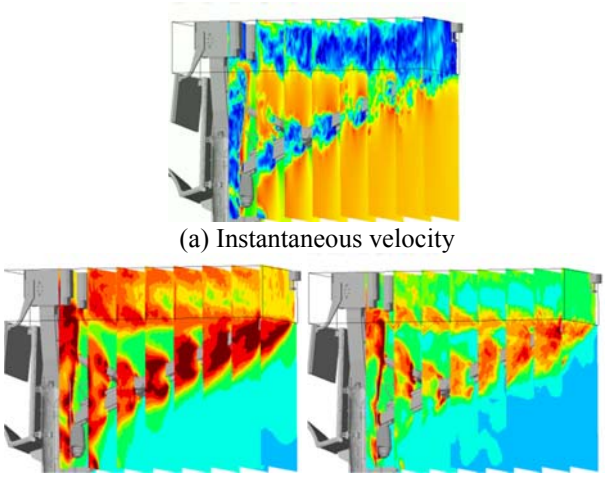

(a) Instantaneous velocity

(b) Bandpass-filtered *Cp* in space

Fig. 9. Instantanious velocity field and the bandpass-filtered *Cp* in space of the fully-dressed configuration around the side-brace and gear bay (left: 141-283Hz, right: 566-1131Hz).

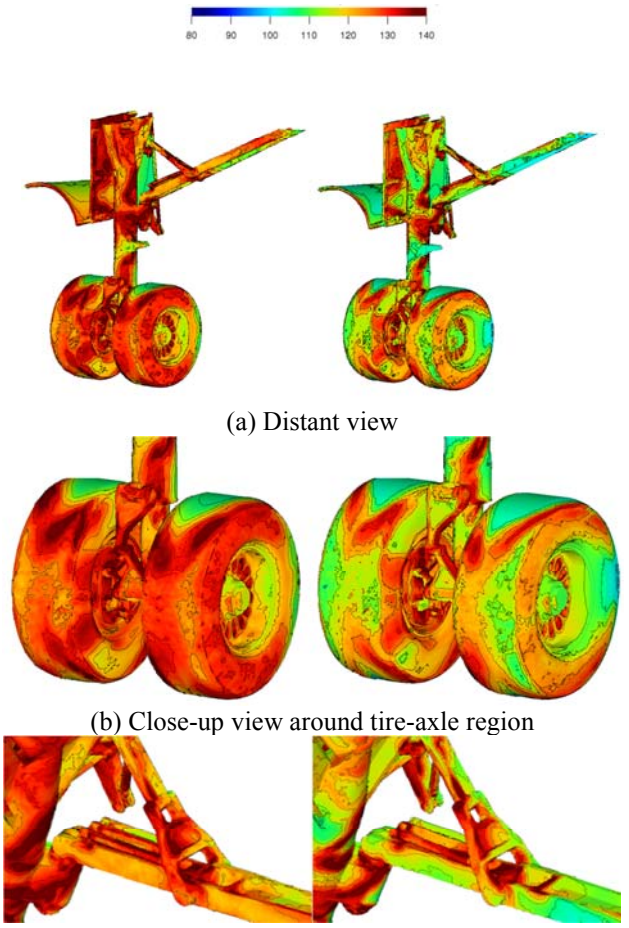

(a) Distant view

(b) Close-up view around tire-axle region

(c) Close-up view around junction between side-brace and lock-link

Fig. 10. Comparison of the bandpass-filtered pressure fluctuation level in dB of the partially-dressed configuration (left: 141-283Hz, right: 566-1131Hz).

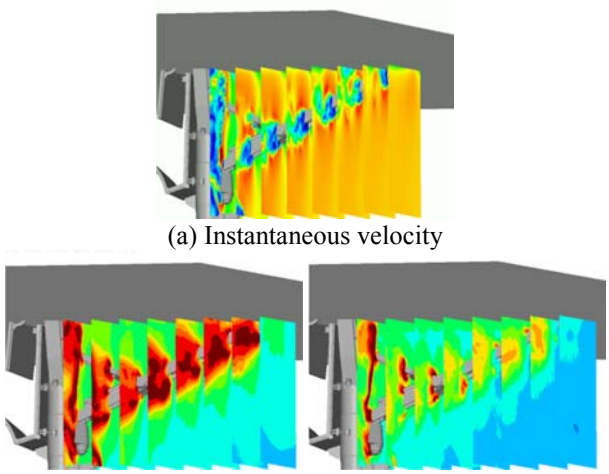

(a) Instantaneous velocity

(b) Bandpass-filtered *Cp* in space

Fig. 11. Instantanious velocity field and the bandpass-filtered *Cp* in space of the partially-dressed configuration around the side-brace (left: 141-283Hz, right: 566-1131Hz).

5.2 Detail investigations on noise generation from tire-axle regions

In this section, the noise generation from tire-axle regions is focused, which has the largest contribution to the noise level. The geometry is simplified without doors, side-brace, and small tubes as shown in Fig. 12 to remove the other excrescence noise sources for the detail investigations. The cavity is also excluded in the geometries. The configuration with the torque-link at backward position is called “baseline” in this section.

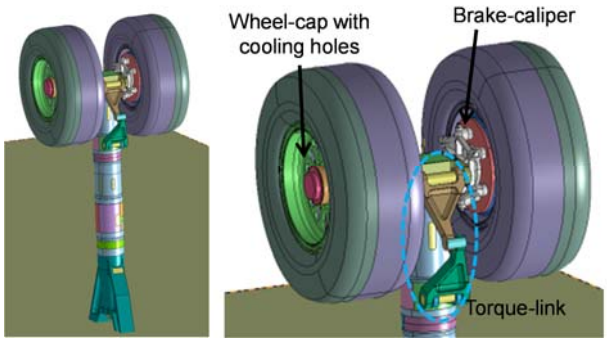

Fig. 12. Simplified research configuration to focus on the tire and bogie noise source without doors, side-brace, and small tubes.

Firstly, influences of detail parts on the flowfield around the tire-axle region were investigated with RANS computations. Figure 13 shows a comparison of the RANS computational results for four configurations from very simplified to precise ones without torque link. The most simplified configuration (i) shows much different from other results for the flow separation from the fore-part of the bogie due to omitting the pin in front of the bogie. By including the cooling holes on the wheels caps, (iii) and (iv), the flow passes from the bogie-side to the outside of wheels through the cooling holes and affects the flow separation on the outer side of wheels. The cooling holes and fidelity of brake caliper also affect the flow acceleration between the tires and the center cylindrical strut, which could be noise sources. The exact geometry shape of the brake caliper (iv) enhances the mixing of shear-layer around the bogie between wheels.

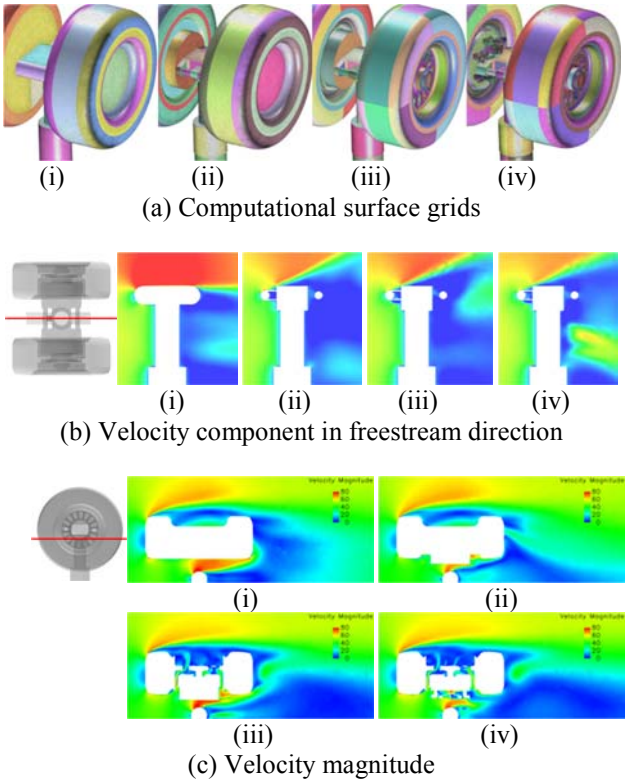

Fig. 13. Comparison of RANS results for the influence of geometry detail on the flowfield ((i) Simplified, (ii) Detailed bogie, (iii) Detailed wheel-cap with cooling holes, (iv) Detailed brake caliper).

The sensitivities of detail parts in the tire-axle regions to the far-field noise are shown in Fig. 14. Figure 14 shows comparison of ΔOASPL from the baseline configuration measured in the wind tunnel test at RTRI. The angles indicate the directivity in the streamwise radiation direction. 0deg means right above the model. The negative and positive angles mean the upstream direction and the downstream direction, respectively. The change of OASPL by the torque link settings is the largest. The sensitivity is about 0.5dB to 1dB. The simplification of the brake-caliper increases noise level, while sealing the cooling holes on the wheel cap reduces the noise level a little. These differences are related to the change in shear-layer mixing and flow separations observed in Fig. 13. These results indicate an expectation that minor geometry changes for each possible noise source around the tire-axle region have possibility to decrease the noise level by around 1dB.

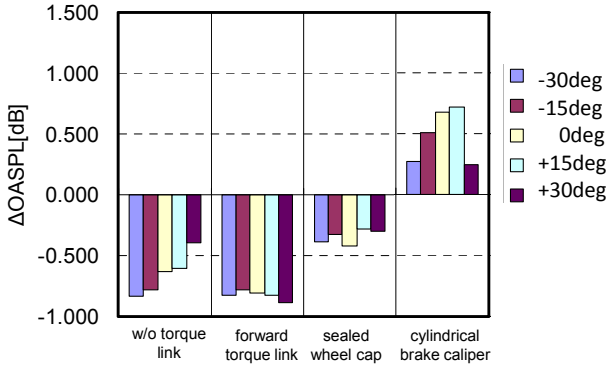

Fig. 14. Comparison of ΔOASPL from the baseline configuration with backward torque link for four selected configurations measured in the wind tunnel test at RTRI.

Next, LES unsteady computations were conducted on the baseline configuration in order to understand the details of the flowfield around the tire-axle region and relation to farfield noise. Figure 15 shows comparison of narrow band spectra of SPL at a microphone location right above the model between experimental and computational result. The computational data are obtained by FW-H using surface pressure of the landing gear with and without the ground plane in the experiment. The FW-H data with the ground plane agrees well with experiment up to 1kHz then gradually decreases its level due to limit of the resolving vortex scale. The difference between with and without ground plane appears in frequency range less than 300Hz, mostly less than 60Hz. This is caused by a flow around the base structure of the model which generates considerable noise reflection at the ground plane in the frequency range.

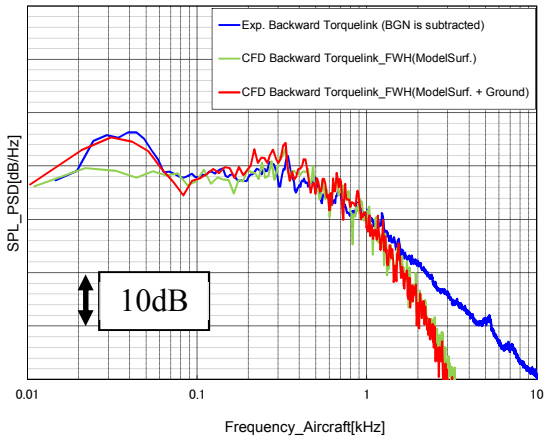

Fig. 15. Comparison of spectra of SPL at a microphone location right above the model between experimental and computational results for the baseline configuration.

Figure 16 shows the computational instantaneous velocity magnitude at sections crossing the center of axle and the center of left tire. The flow largely separates from the fore-part of the bogie toward the ground-side. Flow separations from both upper and lower surface of rear part of the tire are also observed. Figure 17 shows the bandpass-filtered pressure fluctuation level in dB for the frequency range of 141-283Hz and 566-1131Hz on the model surface. Figure 18 shows the instantaneous iso-surfaces of bandpass-filtered *Cp* in space for the frequency range of 40-200Hz and 400-800Hz.

In Fig. 17, the regions with high surface pressure fluctuation level are identified around the inside edges on the back side of tires, the rear part of the side surface of tires, and the junction between the center cylindrical strut, the piston, and torque-link. These regions exist near separation points of boundary layer on the tire or downstream of strong shear-flow by torque-link. The regions with high surface pressure fluctuation level are also identified on the fore-part of the bogie and the protruding objects of the brake caliper. The flow separation from the fore-part of the bogie as shown in Fig. 16 causes the surface pressure fluctuation around the bogie and brake caliper.

The regions with high surface pressure fluctuation level are also identified on the side and piston-side surfaces of the torque-link itself. At lower frequency range, the torque link has high level regions widely on the back-side surface, while the area and level decreases at higher frequency range. Figure 18 at lower frequency range shows that pressure fluctuation in space generated around the junction between the center cylindrical strut and the piston wraps all around the torque link. On the other hand, the result at higher frequency range shows that the pressure fluctuation from the junction has limited impact especially on the side of the torque link.

Figure 19 compares difference of SPL at the microphone located right above the model from the baseline configuration by changing the torque link settings. In the experimental results, results for the no-torque-link and the forward torque-link show 0.5 to 1.0dB reduction of SPL from the baseline configuration over a wide frequency range. The forward torque-link shows a reduction in the wider frequency range. Although some over- and under-estimations are observed in the computational results, the computations capture similar trend in ΔSPL even for such small differences.

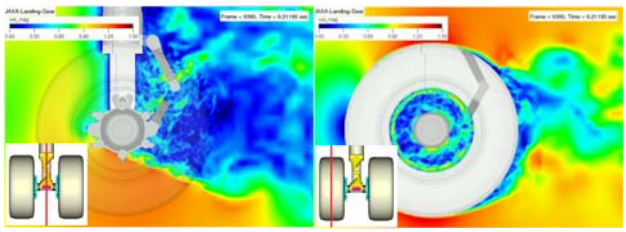

Fig. 16. Instantaneous velocity magnitude around the axle for the baseline configuration.

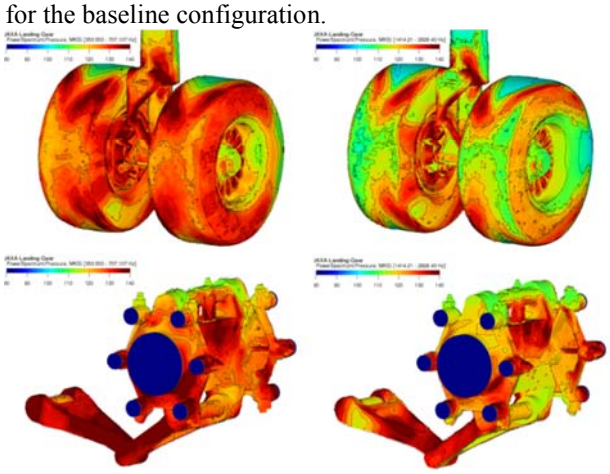

Fig. 17. Comparison of the bandpass-filtered pressure fluctuation level in dB of the baseline configuration (left: 141-283Hz, right: 566-1131Hz).

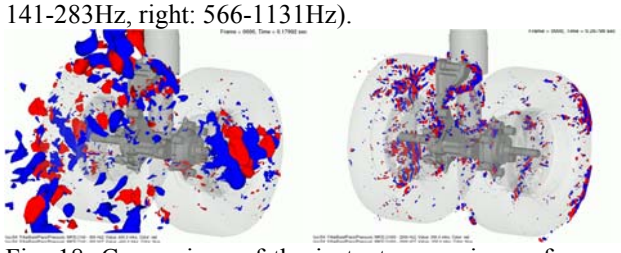

Fig. 18. Comparison of the instantaneous iso-surfaces of bandpass-filtered *Cp* (left: 40-200Hz, right: 400-800Hz).

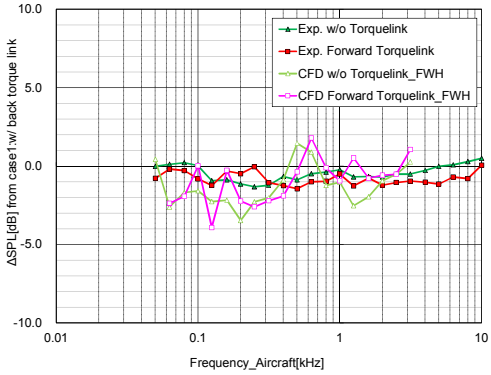

Fig. 19. ΔSPL from the baseline configuration with backward torque link.

Figures 16 and 20 compare instantaneous velocity magnitude at a section crossing the center of axle by the difference of torque link settings. The comparison between the baseline and the no-torque-link configurations shows little difference about the flow separation from fore-part of the bogie. A difference is found in the wake flow after the center cylindrical piston, where high velocity regions exist in the no-torque-link configuration. In the forward torque link configuration, similar high velocity regions like no-torque-link configuration are observed downstream of the piston, whereas the flow separation from the fore-part of the bogie is delayed and the shear-layer is closer to the surface due to accelerated flow around the forward torque-link.

Figures 21 and 22 show the bandpass-filtered pressure fluctuation level in dB for the no-torque-link configuration and the forward-torque-link configuration. The no-torque-link and forward torque-link configurations generally have less pressure fluctuation than the baseline configuration. It is consistent with the noise reduction shown in Fig. 19. On the other hand, the piston of the forward torque-link configuration shows higher level compared to the other case, which is located downstream of the forward torque-link. The aft-part of the bogie also shows higher level in the forward torque-link case, whereas the fore-part of torque-link of the baseline case has much higher level. It is related to the shear-layer of the flow separation is closer to the surface in the forward torque-link case as shown in Figs. 16 and 20. Except for such simple mechanism of the pressure fluctuation due to vortex shedding, the level on the back side of tires is also reduced with the torque-link changes. It is possibly caused by the change of flow between the wheels and/or the cooling air affecting outer side flow of the wheels. Figure 23 compares the mean velocity fields at a section crossing the cooling holes on the wheel cap. The existence of the forward torque link decreases the flow acceleration between the tires and the center cylindrical piston. It also contributes to decrease the pressure fluctuation level around the inner edges of tires.

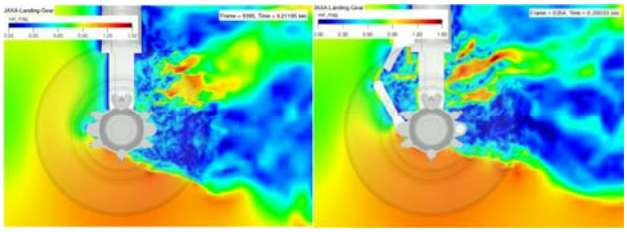

(a) w/o torque-link (b) Forward torque-link

Fig. 20. Instantaneous velocity magnitude around the axle.

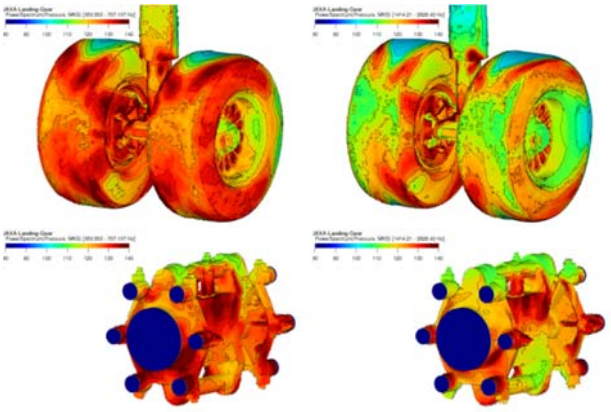

Fig. 21. Comparison of the bandpass-filtered pressure fluctuation level in dB of the configuration without torque-link (left: 141-283Hz, right: 566-1131Hz).

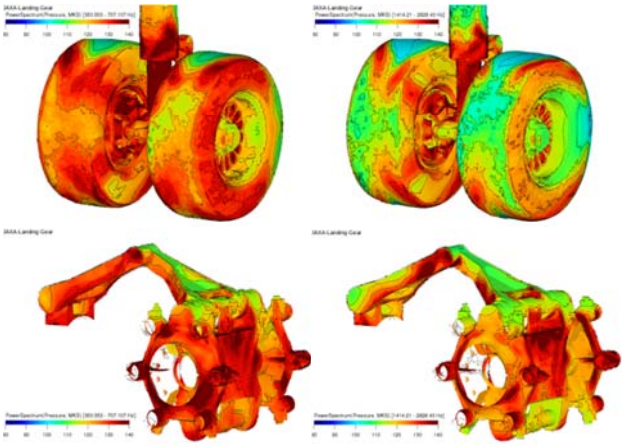

Fig. 22. Comparison of the bandpass-filtered pressure fluctuation level in dB of the configuration with the forward torque-link (left: 141-283Hz, right: 566-1131Hz).

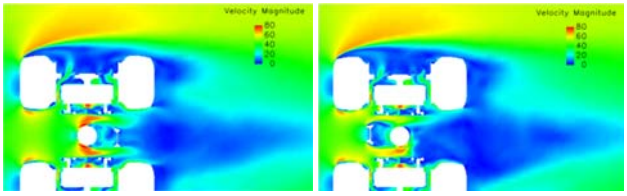

(a)Backward torque-link (b)Forward torque-link

Fig. 23. Comparison of computed mean velocity magnitude at a section crossing the cooling holes.

5.3 Investigations of low-noise fairings around tire-axle regions

In the previous section, it was shown that minor geometry changes for each possible noise source around the tire-axle region have possibility to decrease the noise level by around 1dB, while if further noise reduction is required, another study to apply effective streamlined fairing to cover the all noise sources around the bogie might be required with considering the penalty from operation, safety, and cost problems such as weight, brake cooling, and maintenance accessibility. The flowfield and noise reduction mechanism by the streamlined low-noise fairings around tire-axle regions are investigated by computations. The simplified geometry focused on the tire-axle regions in the previous section is the baseline configuration for the computations. Two types of fairing concepts around the bogie using solid surface and porous surface are investigated in this study. Figure 24 shows the fairings. Both fairings have the same geometry. The porosity of the porous surface fairing is about 60% and the diameter of each hole is 10mm. Compared with the solid surface fairing, the porous surface fairing with holes is expected to have benefits on the weight, brake cooling, and visibility around the bogie for the maintenance.

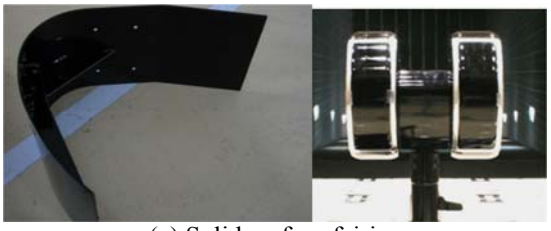

(a) Solid surface fairing

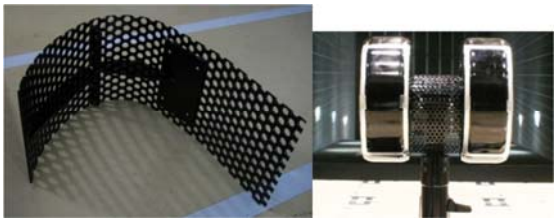

(b) Porous surface fairing

Fig. 24. Low noise fairings around the bogie.

Figure 25 shows noise reduction effects by the fairings which were measured on the fully-dressed configuration by wind tunnel test at a microphone location right above the model. Comparisons of ΔSPL from the baseline configuration without fairing are shown in Fig. 25. The solid surface fairing reduces the noise level by 1~4dB over the frequency range of 300Hz. The porous surface fairing reduces the noise level more under the frequency range of 500Hz, while less over the frequency range of 1000Hz than the solid surface fairing reduces. Figure 26 shows comparison of OASPL at difference microphone locations. The baseline configuration without low-noise fairing has a directivity characteristic to indicate low OASPL right above the model and higher OASPL in the upstream/downstream. OASPL at +30deg direction is the highest. The noise reduction effects by both fairings have similar directivity characteristics.

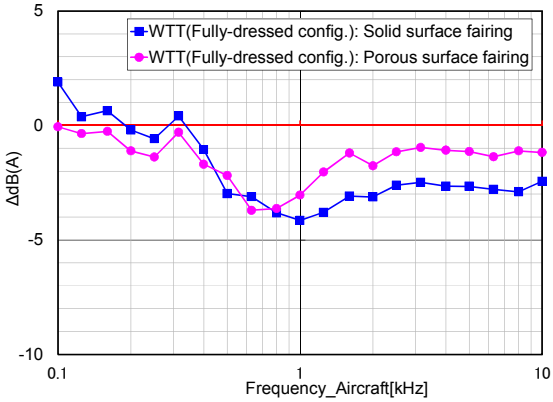

Fig. 25. ΔSPL from the baseline configuration at a microphone location right above the model measured by wind tunnel test (Fully-dressed configuration).

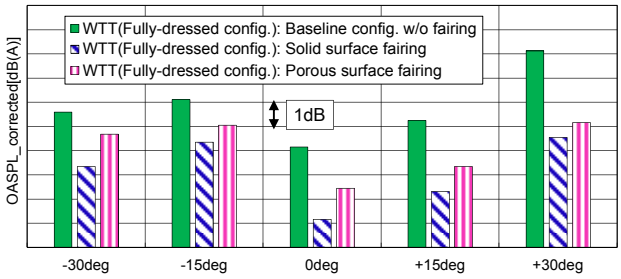

Fig. 26. The directivity of ΔSPL from the baseline configuration measured by wind tunnel test (Fully-dressed configuration).

Figure 27 compares the computed noise reduction effects by the fairings at a microphone location right above the model. Compared with the experimental results as shown in Fig. 25, the computations predict similar trend well on the noise reduction effects by the fairings although the predicted noise reduction effects by both fairings in the computations oscillate especially at lower frequency range and the amounts are much larger than those in the wind tunnel test data. The oscillation may derive from insufficient physical computational time. The measured noise reduction effects by the fairings in Fig. 25 were on the fully-dressed configuration. On the other hands, the computations were conducted on the simplified configuration focused on the noise generation from the tire-axle regions without cavity, doors, side-brace, and small wiring and tubes. The roughly estimated contribution ratio of "Tire-Axle" region to SPL is around 40-50% in our model as shown in Fig. 6. Therefore, it is considered that the noise reduction effects by the wind tunnel test results on the fully-dressed configuration become smaller.

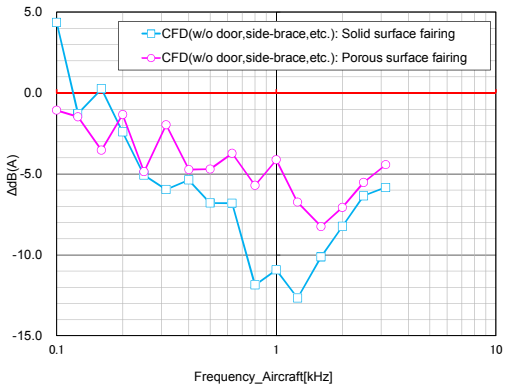

Fig. 27. ΔSPL from the baseline configuration at a microphone location right above the model estimated by CFD.

Figure 28 compares the instantaneous velocity magnitude around the axle at a section crossing near the center of axle and the mean iso-surface of a constant total pressure loss by fairings. Figures 29 and 30 show the bandpass-filtered pressure fluctuation level in space at a section crossing near the center of axle and on the model surface. Both fairings have the same geometry, but generate quite different flowfields.

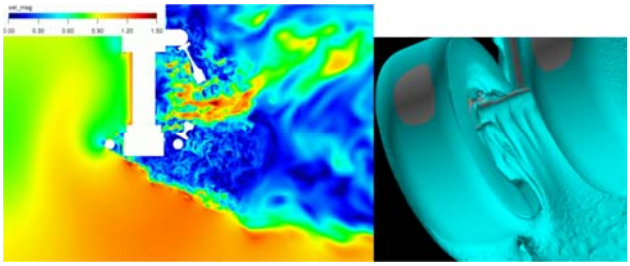

(a) Without fairing

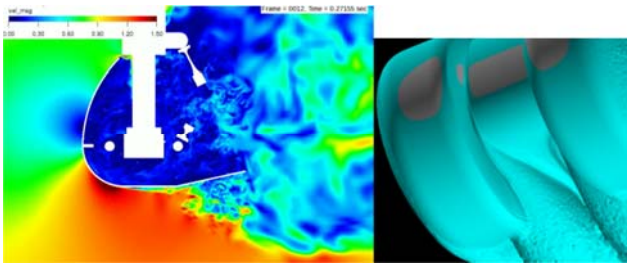

(b) Solid surface fairing

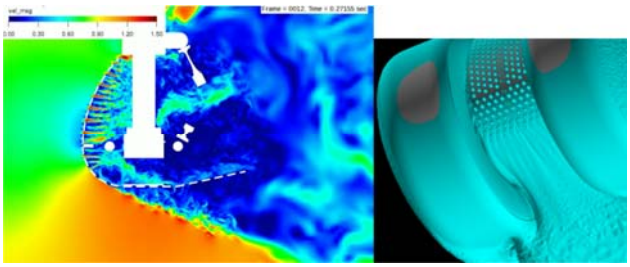

(c) Porous surface fairing

Fig. 28. Comparison of flowfields by fairings (left: computed instantaneous velocity magnitude around the axle at a section crossing near the center of axle, right: mean iso-surface of a constant total pressure loss).

In the case of the baseline configuration without low-noise fairing, the separated flow from the fore-part of the bogie toward the ground-side generates the regions with high pressure fluctuation level. The accelerated and fluctuated flow between the tires and the center cylindrical piston causes high pressure fluctuation around torque-link. The solid surface fairing considerably decreases the pressure fluctuation around the torque-link. In the case of the porous surface fairing, the flow passing in through the porous holes in front of the axle generates pressure fluctuation, but the decreased flow rate around the axle by the fairing results in much less pressure fluctuation around the torque-link, compared with the baseline results. By the fairing effect, the regions with high surface pressure fluctuation level around the torque-link and inner ground contact area of the rear part of the tires are decreased. The fairings

work to decrease the noise sources around the backward torque-link and shield the sound propagation. It is considered that the amount of noise reduction in the downstream direction becomes larger by the fairing and shielding effects.

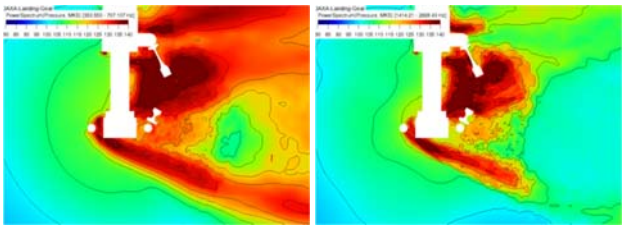

(a) Without fairing

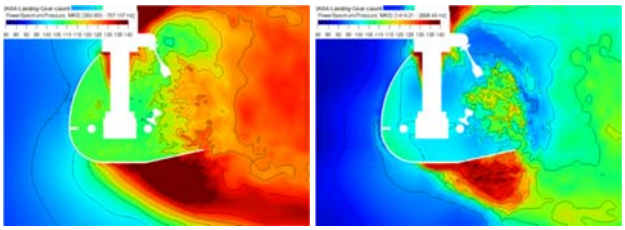

(b) Solid surface fairing

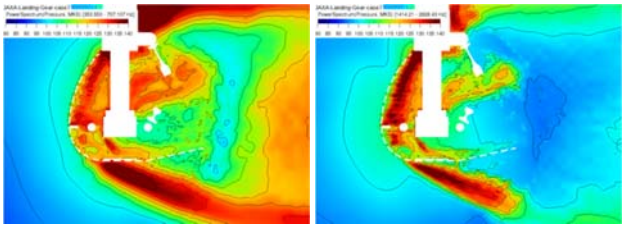

(c) Porous surface fairing

Fig. 29. Comparison of the bandpass-filtered *Cp* in space by fairings (left: 141-283Hz, right: 566-1131Hz).

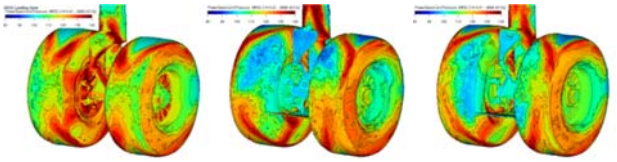

(i) w/o fairing (ii) Solid surface (iii) Porous surface
(a) Forward viewing

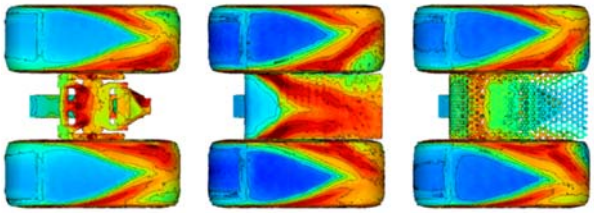

(i) w/o fairing (ii) Solid surface (iii) Porous surface
(c) Viewing from ground-side

Fig. 30. Comparison of the bandpass-filtered pressure fluctuation level in dB by fairings for the frequency range of 566-1131Hz.

By the computational results, it is also shown where to modify to improve the fairings. The solid surface fairing generates the flow separations over the fairing toward the ground-side from the side-edges and rear-part of the fairing, as is shown in Fig. 28. The flow separations also change the flow pattern around lower-inner ground contact area of the rear part of the tires and cause high surface pressure fluctuation on the fairing and ground contact area of the rear part of the tires along the flow separations, especially at lower frequency range. This will be one reason to result in less noise reduction at lower frequency range. Further noise reduction is expected by modifying the geometry of the fairing to suppress the flow separations.

In the case of the porous surface fairing, the flow separations over the fairing from the mid-part of the fairing generate the regions with high surface pressure fluctuation level on the fairing, which are induced by the flow passing through the porous holes. The porous surface fairing also increases the regions with high surface pressure fluctuation level on the ground contact area of the rear part of the tires as is the case with the solid surface fairing as shown in Figs. 30. In addition, locally accelerated flow through the porous holes in front of the axle causes pressure fluctuation as shown in Fig. 29. The flow separations and flow through the porous holes is considered to decrease the noise reduction effect especially in the upstream direction and at higher frequency range. The suppression of the flow separation and optimization of the diameter of the holes will have a potential for further noise reduction comparable to the solid surface fairing.

6. Concluding Remarks

The obtained knowledge and findings by JAXA's recent computational studies on landing gear noise using a two-wheel main landing gear research model has been discussed in this paper.

By the computations on the fully-dressed and partially-dressed configurations, the main noise sources around the two-wheel landing gear model have been investigated with the

experimental results. The prominent possible noise sources on the tire-axle region, side-brace, and doors have been identified.

The detail studies about the flowfield and noise generation mechanism focused on the tire-axle region which was identified to have the largest contribution to the noise level has been conducted. From the computational results, the detailed flow features around the complicated geometry of components around the tire-axle region were clarified. The sensitivity study of detail parts around the tire-axle region to the flowfield and noise level showed that minor geometry changes for each possible noise source around the tire-axle region have possibility to decrease the noise level by around 1dB. The detailed LES computational result gave some useful knowledge such as how torque-link setting affects flowfield and its relation to noise was obtained as well.

In addition, two types of fairing concepts around the bogie using solid surface and porous surface have been investigated. The noise reduction effects and the directivity characteristics were shown by far-field noise measurements in the wind tunnel and numerical simulations. By the computations, it was clarified how the fairings reduce the noise level and where the fairing should be modified to improve the performance.

These knowledge and findings on the detail flowfield and its relation to noise generation will be useful knowledge to search for noise reduction techniques and low noise design of two-wheel type landing gears for aircrafts with wing-mounted engines.

References

[1] Astley, J., "Predicting and Treating Fan and Turbomachinery Noise Current Technology, Research & Facilities," UK-Japan Bilateral Workshop (Aircraft Emissions and Noise), Tokyo, 2006.

[2] Hardin, J. C., "Airframe self-noise: Four years of research; aircraft noise reduction for commercial aircraft," NASA-TM-X-73908, 1976.

[3] Dobrzynski, W., Buchholz, H., "Full-Scale Noise Testing on Airbus landing Gears in the German Dutch Wind Tunnel," AIAA1997-1597, 1997.

[4] Dobrzynski, W., "Almost 40 Years of Airframe Noise Research: What Did We Achieve?," *Journal of Aircraft*, Vol. 47, No. 2, 2010.

[5] Molin, N., Piet, J. F., Chow, L. C., Smith, M. G., Dobrzynski, W. M. and Seror, C., "Prediction of Low Noise Aircraft Landing Gears and Comparison with Test Results," AIAA 2006-2623, 2006.

[6] Herkes, W. H., Olsen, R. F., and Uellenberg, S., "The Quiet Technology Demonstrator Program: Flight Validation of Airplane Noise-Reduction Concepts," AIAA 2006-2720, 2006.

[7] Elkoby, R., Brusniak, L., Stoker, R., Khorrami, M. R., Abeysinghe, A., and Moe, J., "Airframe Noise Test Results from the QTD II Flight Test Program," AIAA 2007-3457, 2007.

[8] Ravetta, P. A., Burdisso, R. A., Ng, W. F., Khorrami, M. R. and Stoker, R. W., "Screening of Potential Noise Control Devices at Virginia Tech for QTD II Flight Test," AIAA 2007-3455, 2007.

[9] Khorrami, M. R., Lockard, D. P., Humphreys, W. M., Jr., Choudhari, M. M., and Van de Ven, T., "Preliminary Analysis of Acoustic Measurements from the NASA-Gulfstream Airframe Noise Flight Test," AIAA 2008-2814, 2008.

[10] Neuhart, D.H., Khorrami, M.R., and Choudhari, M.M., "Aerodynamics of a Gulfstream G550 Nose Landing Gear Model," AIAA2009-3152, 2009.

[11] Zawodny, N.S., Liu, F., Yardibi, T., Cattafesta, L., Khorrami, M,R., Neuhart, D.H., Van de Ven, T., "A Comparative Study of a ¼-scale Gulfstream G550 Aircraft Nose Gear Model", AIAA2009-3153, 2009.

[12] Van de Ven, T., Louis, J., Palfreyman, D., Mendonça, F., "Computational Aeroacoustic Analysis of a ¼ scale G550 Nose Landing Gear and Computation to NASA & UFL Wind Tunnel Data", AIAA2009-3359, 2009.

[13] Yokokawa, Y., Imamura, T., Ura, H., Kobayashi, H., Uchida, H., and Yamamoto, K., "Experimental Study on Noise Generation of a Two-Wheel Main Landing Gear," AIAA2010-3973, 2010.

[14] Imamura, T., Hirai, T., Yokokawa, Y., Murayama, M., and Yamamoto, K., "Aerodynamic and Aeroacoustic Simulations of a Two-wheel Landing Gear," *Procedia Engineering, Proc. of IUTAM Symposium on Computational Aero-Acoustics for Aircraft Noise Prediction*, Vol. 6, pp. 293-302, 2010.

[15] Murayama, M., Yokokawa, Y., Kato, H., Ura, H., Uchida, H., Yamamoto, K., Abe, K. and Wu, L., "Computational and Experimental Study on Noise Generation from Tire-Axle Regions of a Two-Wheel Main Landing Gear," AIAA2011-2821, 2011.

[16] Yamamoto, K., Murayama, M., Yokokawa, Y., Ura, H. and Imamura, T., "Experimental and numerical study on a two-wheel main landing gear noise," *Proc. of inter-noise 2011*.

[17] Murayama, M., Yokokawa, Y., Yamamoto, K., and Hirai, T., "Numerical Simulation of a Two-Wheel Main Landing Gear with Low-Noise Fairings around Tire-Axle Region," AIAA2012-2279, 2012.

[18] Ito, T, Ura, H., Nakakita K., Yokokawa, Y., Ng, W., Burdisso, R., "Aerodynamic/Aeroacoustic testing in Anechoic Closed Test Sections of Low- Speed Wind

Tunnels," AIAA2010-3750, 2010.
[19] Maeda, T., and Kondo, Y., "RTRI's Large-scale Low-noise Wind Tunnel and Wind Tunnel Tests," Quarterly Report of RTRI, Vol.42, No.2, pp.65-70, 2001.
[20] Murayama, M. and Yamamoto, K., "Comparison Study of Drag Prediction by Structured and Unstructured Mesh Method," *Journal of Aircraft*, Vol.45, No.3, 2008, pp. 799-822.
[21] Yamamoto, K., Tanaka, K., Murayama, M., "Comparison Study of Drag Prediction for the 4th CFD Drag Prediction Workshop using Structured and Unstructured Mesh Methods," AIAA Paper 2010-4222, Jun. 2010.
[22] Nakahashi, K., Ito, Y., and Togashi, F, "Some challenges of realistic flow simulations by unstructured grid CFD", *International Journal for Numerical Methods in Fluids*, Vol.43, 2003, pp.769-783.
[23] Ito, Y. and Nakahashi, K. "Direct Surface Triangulation Using Stereolithography Data," *AIAA Journal*, Vol. 40, No. 3, pp. 490-496, 2002.
[24] Ito, Y. and Nakahashi, K., "Surface Triangulation for Polygonal Models Based on CAD Data," *International Journal for Numerical Methods in Fluids*, Vol. 39, Issue 1, pp. 75-96, 2002.
[25] Sharov, D. and Nakahashi, K., "A Boundary Recovery Algorithm for Delaunay Tetrahedral Meshing," Proceedings of 5th International Conference on Numerical Grid Generation in Computational Field Simulations, 1996, pp. 229-238.
[26] Ito, Y. and Nakahashi, K., "Improvements in the Reliability and Quality of Unstructured Hybrid Mesh Generation," *International Journal for Numerical Methods in Fluids*, Vol. 45, Issue 1, May 2004, pp. 79-108.
[27] Ito, Y., Shih, A., Soni, B., and Nakahashi, K., "An Approach to Generate High Quality Unstructured Hybrid Meshes," AIAA Paper 2006-0530, Jan. 2006.
[28] Noelting, S., Bres, G., and Dethioux, P., "A Hybrid Lattice-Boltzmann/FW-H Method to Predict Sources and Propagation of Landing Gear Noise," AIAA Paper 2010-3976, 2010.
[29] Fares, E. and Noelting, S., "Unsteady Flow Simulation of a High-Lift configuration using a Lattice Boltzmann Approach," AIAA Paper 2011-0869, 2011.

Copyright Statement